ELSEVIER

Physics of the Earth and Planetary Interiors 134 (2002) 53–69

PHYSICS OF THE EARTH AND PLANETARY INTERIORS

www.elsevier.com/locate/pepi

Seismic tomographic images of the cratonic upper mantle beneath the Western Superior Province of the Canadian Shield—a remnant Archean slab?

S. Sol [a], C.J. Thomson [a,*], J.-M. Kendall [b], D. White [c], J.C. VanDecar [d], I. Asudeh [c]

[a] *Department of Geological Sciences & Geological Engineering, Queen's University, Kingston, Ont., Canada K7L 3N6*
[b] *School of Earth Sciences, University of Leeds, Leeds LS2 9JT, UK*
[c] *Geological Survey of Canada, 615 Booth St., Ottawa, Ont., Canada K2A 0Y3*
[d] *Department of Terrestrial Magnetism, Carnegie Institution of Washington, Washington, DC 20015, USA*

Received 28 June 2002; accepted 1 July 2002

Abstract

Knowledge of the velocity structure of the upper mantle beneath the Western Superior Province (WSP) is key to understanding better the accretionary processes active during the Archean. To that end, teleseismic P- and S-wave travel times recorded as part of the Teleseismic Western Superior Transect (TWST) were inverted for their respective seismic velocities. This experiment involved 17 portable broadband stations arrayed in northern Ontario, Canada, so as to cross-cut the strike of many subprovinces as well as the boundary with the Proterozoic Trans-Hudson Orogen to the north. The 5-month deployment yielded 1423 P-wave and 651 S-wave high-quality residuals for inversion. The resulting tomographic images reveal three apparently-robust velocity anomalies represented by: (i) a dipping tabular high-velocity anomaly; (ii) a relatively shallow low-velocity anomaly directly above the positive anomaly; and (iii) a deep low-velocity body. The first anomaly may be interpreted in the Western Superior context as a 30–50 km thick eclogite/dunite layer representing remnant subducted oceanic lithosphere. The presence of such a body within the cratonic root would suggest its origin at around 2.7 Ga and the apparent SE–NW strike is noticeably oblique to the main EW trend of the subprovince boundaries. The low-velocity anomalies may be related to processes that occurred at the edges of the descending slab or they may be expressions of later upwelling material. The presence of a thick cratonic root (≈300 km) may also be revealed by the tomographic images. Overall, these travel time results are considered compatible with late Archean structures at depth resembling those of modern subduction tectonics, though other possibilities (e.g. small-scale convection cells) exist.

Keywords: Seismic tomography; Superior Province; Canadian Shield; Upper mantle; Archean tectonics

1. Introduction

The Superior Province of the Canadian Shield, the world's largest region of Archean (actually 3.0–2.7 Ga) rocks, is characterized towards the west by an east–west trending pattern of alternating meta-sedimentary and granite–greenstone volcanic belts, perhaps explained by a particular tectonic model of terrane accretion (Langford and Morin, 1976). This model suggests that the subprovinces comprise a series of island arcs and adjoining basins accreted along successive northward-dipping subduction zones. Since

* Corresponding author. Tel.: +1-613-533-6592; fax: +1-613-533-6178.
E-mail address: thomson@geol.queensu.ca (C.J. Thomson).

0031-9201/02/$ – see front matter
PII: S0031-9201(02)00081-X

its formation at around 2.7 Ga, this part of the Canadian Shield has been affected by only minor deformations, rendering it an important area to test such accretionary models explaining the assembly and stabilization of cratonic Archean lithosphere.

Several large-scale shear-velocity models of the upper mantle beneath the Canadian Shield have been established already using travel times of S and SS (Grand and Helmberger, 1984) and phase velocities of Rayleigh and Love waves (Brune and Dorman, 1963; see also Fouch et al., 2000). These shear-wave models contain a fast mantle lid 120–150 km thick overlaying a low-velocity zone down to a depth of approximately 300 km. To refine these lithospheric velocity models within the Western Superior Province (WSP; Fig. 1), a portable teleseismic experiment was undertaken during the period May to mid-November 1997. Part of the Canadian Lithoprobe project's Western Superior transect (WST), the Teleseismic Western Superior Transect (TWST) experiment consisted of a temporary seismic array of 14 broadband stations deployed along a 480 km line from west of Thunder Bay to north of Pickle Lake. Three additional stations were located still further north in order to span the Archean–Proterozoic transition (Superior Province/Trans-Hudson Orogen; see Fig. 1). Complementary geophysical studies have also been conducted along the main 480 km corridor to better understand the velocity structure of the crust and shallow upper mantle (White et al., 1999; Musacchio et al., 1999; Hynes, 1999).

Our model volume spans the region between latitude 48–56°N and longitude 85–92°W, extending to a depth of 900 km. The teleseismic records have been used previously to estimate the effective upper mantle anisotropy beneath the craton (Kay et al., 1999). The

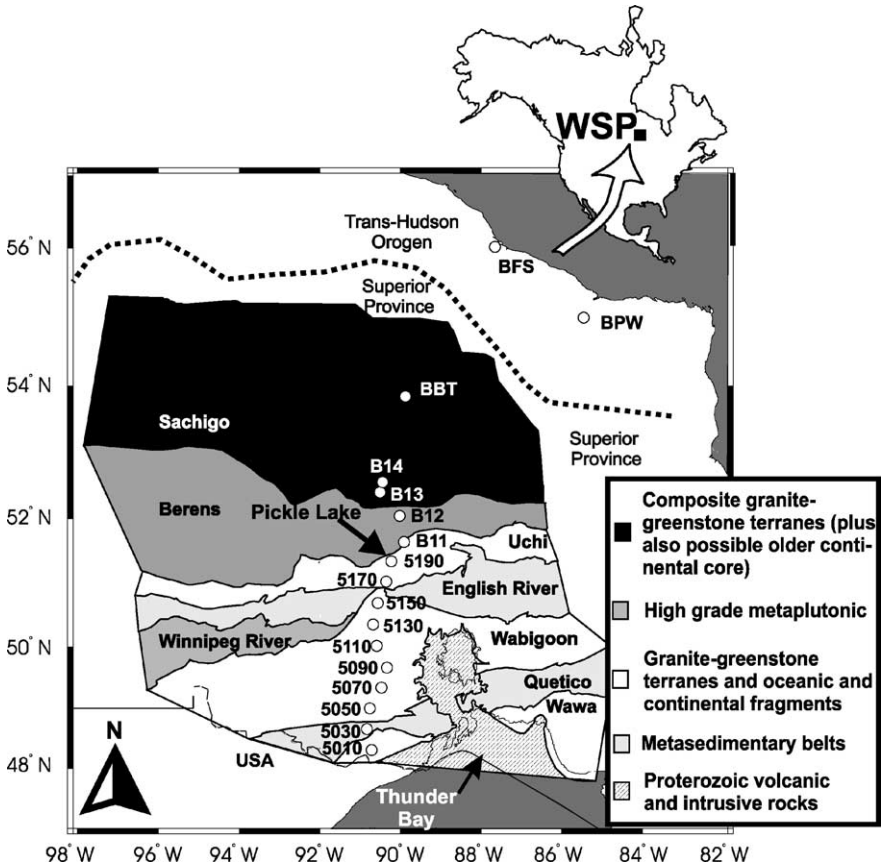

Fig. 1. Geological map of the study area illustrating the broadband seismic station locations used (black circles with white centers).

objective of this paper is to investigate the deeper (sub-crustal) velocity structures using direct P- and S-wave teleseismic travel time tomography.

2. Data selection

Circa 1100 globally-distributed earthquakes were recorded during the experiment, from which we first selected a subset of approximately 300 events with magnitudes larger than 4.9 and epicentral distances ranging from 30 to 130°. From these earthquakes, two groups of 158 and 76 with the clearest waveforms were chosen for the travel time analysis of compressional and shear-wave phases, respectively. The distributions of these events (Fig. 2) provide wide coverages in azimuth and epicentral distance for both wave types. Core phases PKP and SKS were included in the analysis.

This selection lead to 1423 P-wave and 651 S-wave teleseismic travel times that were inverted. As a result of technical problems, stations B13 and BBT located in the Sachigo subprovince and the station BFS located in the Trans-Hudson Orogen were recording only intermittantly, though they contributed valuable data during those times.

3. Methodology

Once events with clear waveforms on all recordings were identified, and in order to facilitate the phase picking, each earthquake record was further processed using bandpass filters to reduce the noise and the low-frequency content. Two-pass, two-pole Butterworth filters were used with a passband for most of the events of 0.4–2 Hz for P-waves and 0.04–0.16 Hz for S-waves.

The determination of the relative delay times and the inversion algorithm employed in this study are essentially as described by VanDecar (1991). The travel time residuals are assessed relative to the IASP91 reference Earth model (Kennett and Engdahl, 1991) using a multi-channel cross-correlation technique (VanDecar and Crosson, 1990). For each selected earthquake, a search for the maximum waveform cross-correlations between all possible pairs of traces is used to estimate relative delay times. This waveform coherency method has the advantage that it permits the identification and rejection of noisy traces in a semi-automatic way. The relative delay times measured this way have an estimated standard error of 0.02 s for P-waves and 0.05 s for S-waves (both slightly rounded up). These may be compared, for example, with the values quoted by

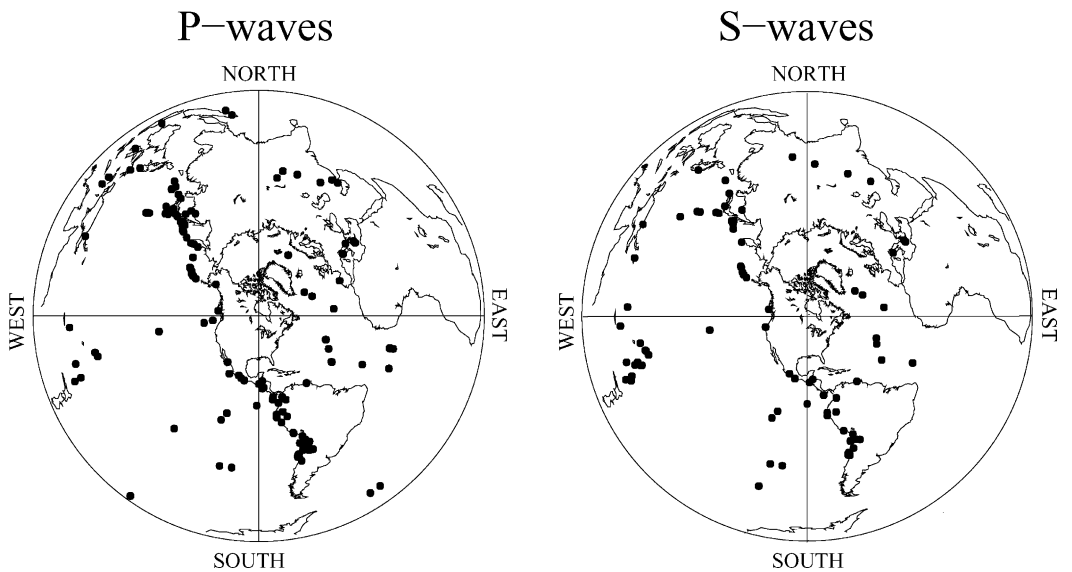

Fig. 2. Azimuthal projection of the distributions of earthquakes used in the determination of the relative delay times. Plotted as filled circles are a total of 158 events used in the P-wave inversion (left) and 76 events used in the S-wave inversion (right).

Rondenay et al. (2000) and we emphasize that these error estimates simply provide a compact representation of waveform clarity and consistency across the array for each event. They are not used to regularize or halt iterations of the inversion procedure described below. After several data-winnowing passes and the resolution tests to be described, we believe that all reasonable estimates of the relative delay time uncertainty will have a smaller impact on final model reliability than do other uncertainties in the method (e.g. due to structures outside our assumed model volume).

The next step is to parameterize P- and S-wave slowness structures using splines under tension over a dense grid of knots (Cline, 1981). The interpolation between the slowness values at each knot creates a smooth model and thereby allows ray tracing. The grid is composed of 35 knots in depth, 43 in latitude and 29 in longitude, for a total of 43,645. The knot spacing is not uniform, being somewhat coarser towards the edges of the volume and at depth, and being as low as 33 km in the central (resolved) region.

Finally, the two datasets of relative arrival times are inverted for three-dimensional subcrustal velocity models beneath the transect. Naturally the best resolution will be in a corridor defined by the array of stations. The non-linear inversion procedure simultaneously solves for the slowness perturbations, station terms (to account for local crustal structure including station elevations) and earthquake mislocations (which also accounts, to first order, for structure far from the network). For the images presented, the station static corrections were not damped in order to minimise the possibility that crustal structure was mapped into the mantle. In tests with various degrees of station-term damping, the images remain qualitatively unchanged. For example, the shallow low-velocity feature Z in Fig. 7 actually becomes somewhat sharper if the crustal corrections are damped, suggesting that the mantle images are resilient.

The teleseismic relative delay time data are insensitive to the average velocity structure at each depth and so the variations that we observe are undoubtedly embedded in a poorly-constrained radial background structure (e.g. one that could be imaged in a larger-scale, lower horizontal-wavenumber study). This is a basic limitation of the regional tomography method which we must accept.

To address the non-linearity problem, we employ, iteratively, three-dimensional ray tracing, revision of travel time partial derivatives with respect to slowness parameters and robust inversion of the updated system of linearized equations. The ‘robust inversion’ involves downweighting equations associated with high residuals and use of the conjugate-gradient algorithm to obtain a convergent solution. In our presented images, we have chosen 11 iterations with downweighting of equations and each iteration uses 2000 conjugate gradient steps. The iterations are interrupted when the slowness perturbations (i.e. the anomalous structures) do not show any significant variation from the previous iteration (in practice this is after 10 or 11 steps, but we have experimented with up to 20 iterations to verify stability of the images in extreme cases). We have noted that the broad features of the model are seen to be present, and more than half of the data rms is satisfied, after only the first or second iteration. As the iterations proceed the image in the best-resolved central region of the model volume tends to become smoother (i.e. the highs and lows become less extreme).

We have also examined the effects, on more heavily damped linear inversions, of suppressing source relocations and grid-periphery slowness anomalies. Source location errors create linear trends across the array which prohibit good fits to the data, but which do not substantially affect the models. Suppressed peripheral slowness anomalies map into the central region, but the essential features of our images are preserved.

Overall we can say that by using either simple linear or the iterative robust inversion with source, receiver and peripheral model parameters, we can straighforwardly obtain rms reductions of 60 to 90+% (i.e. down to about the estimated uncertainty level of the travel time measurements). All the images are qualitatively similar, with the robust inversion strategy yielding the smoothest anomalies in the best-resolved central region. For this reason, we consider that each final model obtained using this VanDecar (1991) ‘robust’ approach should represent a minimal velocity structure consistent with the travel time perturbations observed across the WSP. Independent inversions were obtained for compressional- and shear-wave slowness (or velocity) models.

4. Resolution

Further to the data-fitting issues of Section 3, and prior to discussing the images resulting from our measurements, it is important to assess the likely resolution, which depends mainly on the sufficiency of crossing rays within our model space. We present two resolution tests, one the familiar 'checkerboard' test (Fig. 3a and b) and the other a 'slab' model (Figs. 4a–6a). The first test model (Fig. 3) is similar to that used by Bank et al. (1998) and consists of a pattern of alternating positive and negative localized velocity anomalies. It should characterize the ability of the inversion to recover velocity structures with length scales ≈100 km throughout the entire three-dimensional volume. For scales an order of magnitude less than this we know that our data will not have satisfactory resolution anywhere and for scales of 50–100 km a checkerboard pattern is already challenging. Although instructive, ultimately we do not consider this to be the only important resolution test pattern, so we choose to display just the recovered P-wave images (Fig. 3). Our second test model was constructed with reference to the position of anomalies seen in preliminary real-data inversions. This 'synthetic slab' model is comprised of three velocity perturbations: (i) a tabular high-velocity body (+3%) extending from a depth of 70 km to a depth of 700 km and characterized by a dip angle of 60°, a thickness of 50 km and a strike direction of 325° from north; (ii) a shallow low-velocity anomaly (−4%) represented by a sphere centered at 200 km depth; and (iii) a deep low-velocity anomaly (−3%) represented by a sphere centered at 500 km depth. Both spheres have a radius of 120 km and are located, respectively, in the eastern and central part of the Wabigoon subprovince.

Synthetic data were generated for each known model by using the linearized approximation based on the rays of the IASP91 starting model. Gaussian noise with standard deviation of 0.1 s (cf. Bank et al., 1998) was added. This significantly exceeds the estimated uncertainties in the travel time measurements, but it seems reasonable when receiver/crustal, source mislocation and exterior velocity–structure contributions are accounted for. The regularization applied was the same as that used for the real-data inversions and it was derived from a trade-off curve in order to simultaneously minimize the synthetic data misfit and the roughness of the image. As a result of this smoothing the recovered models significantly underestimate the magnitude of the velocity anomalies.

Several inferences can be drawn from the results of the checkerboard test(s) (Fig. 3a). Both the P- and S-wave (the latter not shown, as explained above) recovered models indicate that seismic-velocity structures on this scale and within the area (48–53°N, 90–92°W) are resolvable in the upper part of the lithosphere (i.e. beneath the main station profile down to 200 km). The high–low pattern is also reasonably recovered at around 400 km depth along profile CD in Fig. 3a. In other words, the portion of the models between 200 and 500 km depth is better resolved slightly to the east than it is directly below the main NS receiver line. (The same is likely true to the west, from source location considerations, but we focus on the east in view of the structures inferred from the real data.) There is more diagonal smearing, particularly towards the south, in section AB at these depths. These observations suggest that we have a certain degree of out-of-receiver-plane resolution. Smearing effects, which alternating patterns on this length scale can reveal, are clearly present, but the results are encouraging for a quasi-linear array such as this. Indeed, selecting a smaller number of somewhat larger spheres shows them to be substantially more recoverable.

Overall, for the checkerboard P-wave images in Fig. 3a, the structures located under the southern (mainline) part of our seismic array are reasonably resolved between 70 and 400+ km depth. The corresponding S-wave images (not shown) recover the anomalies only in the top 200 km. At 300 km, the S-waves order the highs and lows correctly on moving south to north, but the (diagonal) depth smearing is more significant and especially so towards the south. Unfortunately, the northern part of the Sachigo subprovince and the area beneath the Trans-Hudson Orogen are poorly recovered with either P- or S-waves as a result of the sparcity of receivers north of 53°.

Fig. 3b shows a variant checkerboard test with highs/lows aligned along the section MN shown in Fig. 3a (i.e. in a vertical plane containing the potential 'slab' structure's dip—see below). The recovered spheres labeled 1–2 and 4–8 are correctly positioned and we note that smearing towards the NE does not cause them to effectively merge (thereby suggesting a 'slab') or cancel. For spheres 3 and 4, smearing

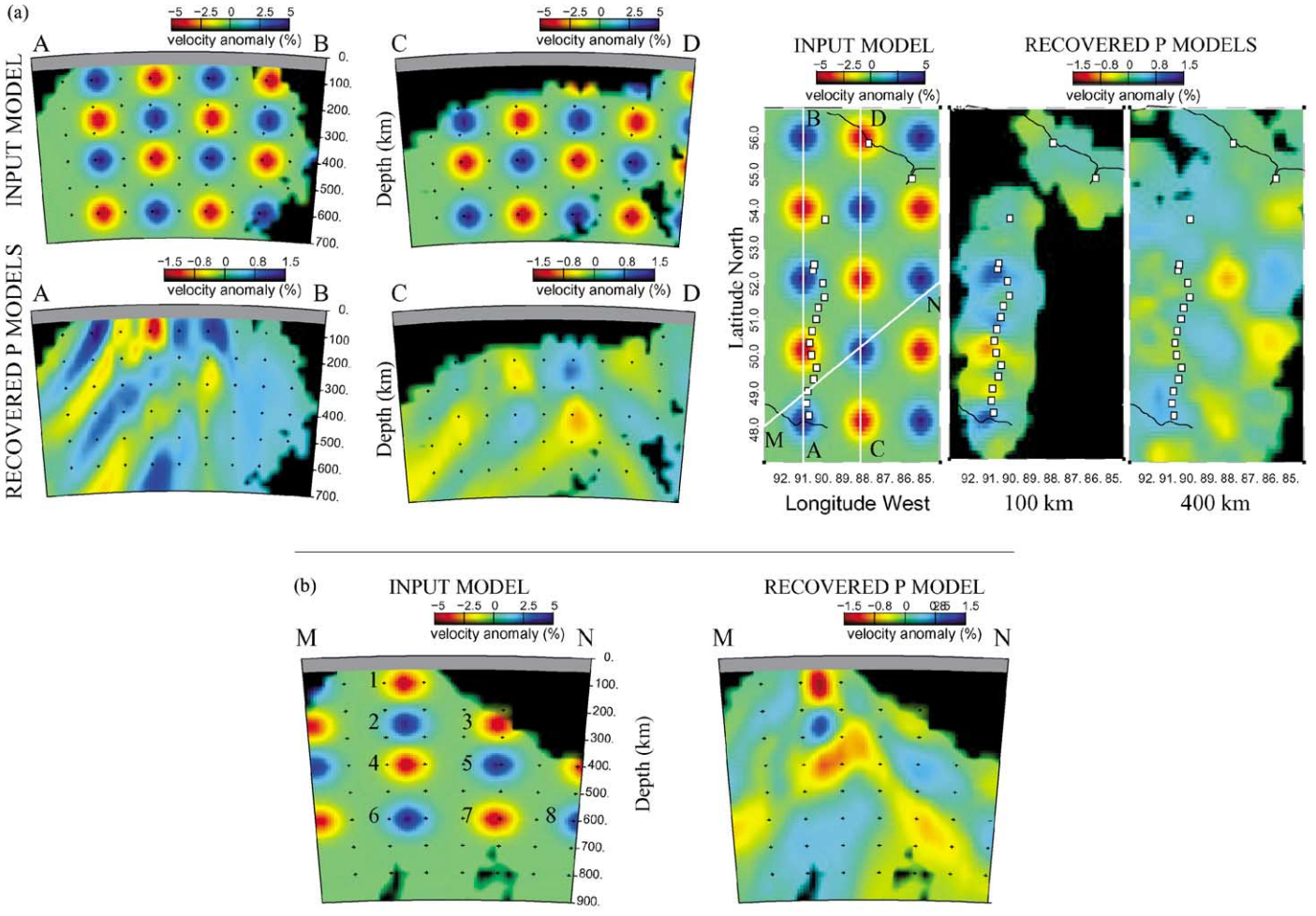

Fig. 3. (a) Sections through the input and output synthetic checkerboard resolution test images (only the P-wave results are presented). We show on the left four vertical sections with the input models (top) and recovered models (bottom). On the right are horizontal sections with the input model (first) and the recovered models at 100 km (second) and at 400 km (third, far right). The areas shaded black signify poor ray coverage (actually a low ray hit count, which implies poor resolution). Vertical resolution is also poor in the horizontal band shaded grey in the upper part of the images: since all rays are nearly vertical here, there is a trade-off between crustal statics (or station corrections) and mantle structure just below Moho. The positions of the stations are represented by white squares and the locations of the vertical cross-sections are shown by white lines in the first horizontal depth section. (b) Vertical sections through the input (left) and output (right) synthetic checkerboard resolution test images along the direction MN of the tabular anomaly observed in the real-data images (e.g. Fig. 7).

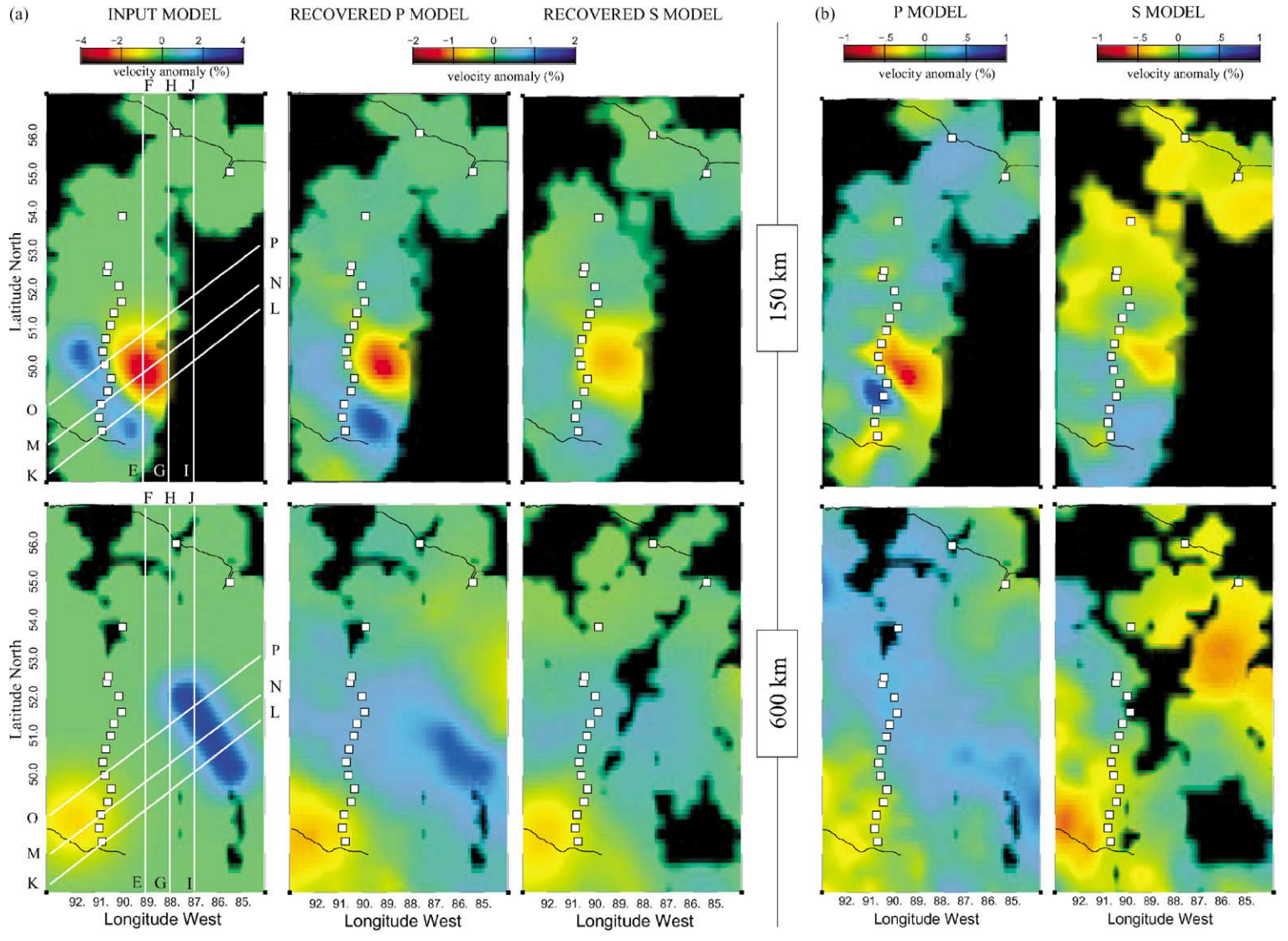

Fig. 4. Horizontal sections: (a) input and recovered P- and S-wave models from the slab resolution test at depths of 150 km (top row) and 600 km (bottom row); (b) horizontal sections across the P- and S-wave real-data models at 150 km (top row) and 600 km (bottom row). The areas shaded black signify poor ray coverage or resolution and the locations of the stations are represented by white squares.

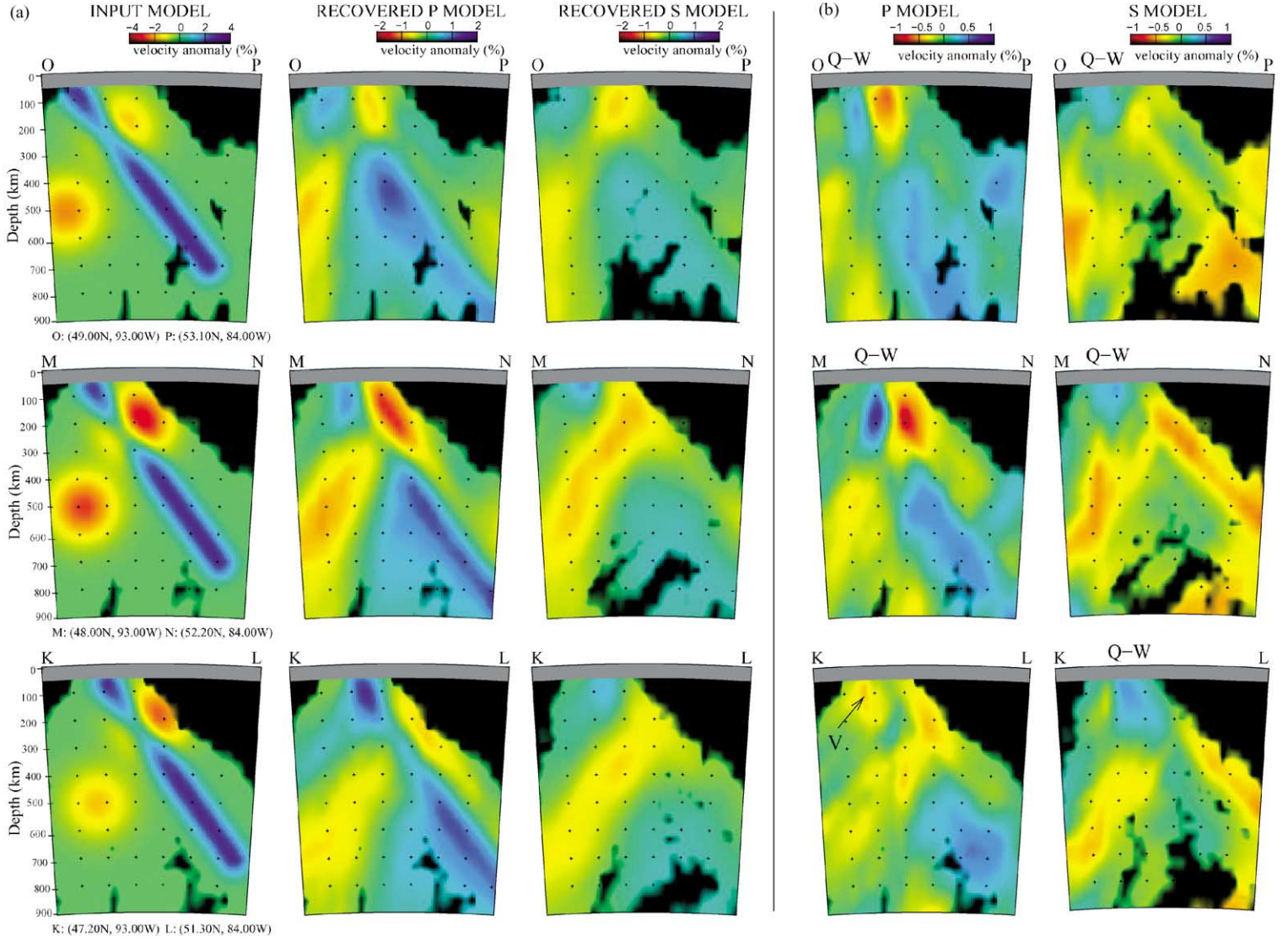

Fig. 5. Vertical sections perpendicular to the strike of the hypothesized subducted slab: (a) input and recovered P- and S-wave models from the slab resolution test; (b) sections across the P- and S-wave real-data models. The locations of the vertical cross-sections are shown by white lines in the first horizontal sections (Fig. 4a).

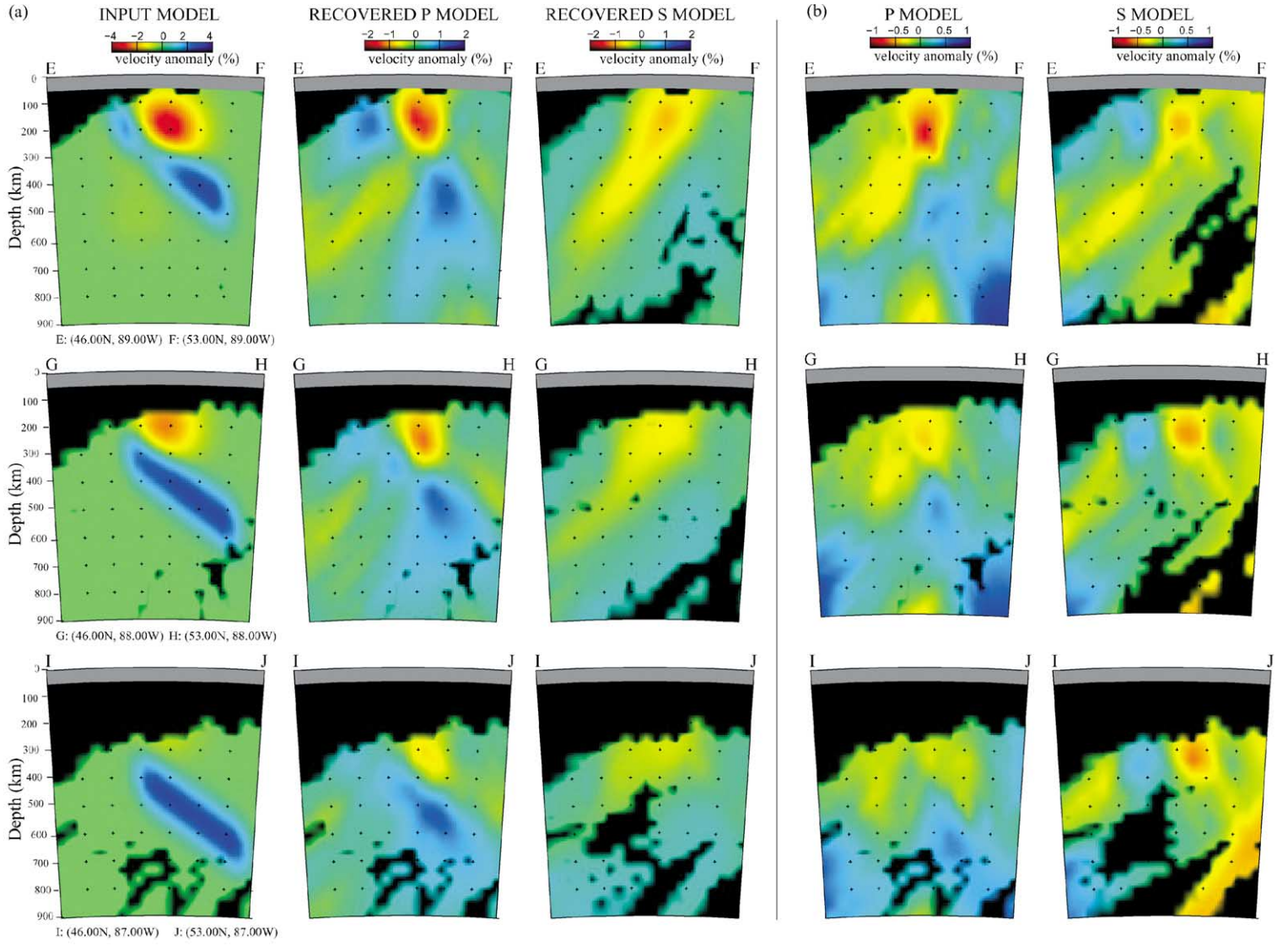

Fig. 6. Vertical sections through the dipping slab in the NS direction: (a) input and recovered P- and S-wave models from the slab resolution test; (b) sections across the P- and S-wave real-data models. The locations of the vertical cross-sections are shown by white lines in the first horizontal sections (Fig. 4a).

is actually most pronounced in the direction roughly orthogonal to the dip of the possible slab (i.e. towards the SW). This is presumably caused by a combination of the northern stations (e.g. BBT) being somewhat isolated and the importance of data from the south for the sphere 3, which lies on the northern edge of the region defined as 'resolved' by the ray coverage information and so is poorly reconstructed. Sphere 7 at depth is smeared to the NE, whereas sphere 6 is smeared to the SW. It is encouraging that the ordering of all the highs and lows at this depth level is correctly reproduced.

From the results of the 'synthetic slab' test(s) the following observations can be made (Figs. 4a–6a). The shallower part of the slab (down to 200 km) is reasonably-well recovered in the P-wave model and somewhat less so in the S-wave model (Fig. 5a). Over this depth range its strike is better resolved (see Fig. 4a; P-wave image at 150 km) than its dip, which from the Fig. 5a frames seems to be slightly towards the north (although if one had only section MN of the P-wave image in Fig. 5b it might be taken to dip vertically). The shallow low-velocity sphere located somewhat east of the station line is quite poorly resolved (smeared) in the S-wave model in comparison with its image in the P-wave model (compare the MN sections for P- and S-waves in Fig. 5a). Regarding the deeper part of the slab (from 300 to 700 km), its dip angle and its localization are much better reproduced by the P-wave image than by the S-wave one, which shows very poor recovery. Other resolution tests were performed to check how well constrained the dip of the slab is after inversion. These tests indicated that the dip observed in our real-data P-wave images should be resolved to $\pm 5^{\circ}$. Below about 500 km, the P-wave data lateral and vertical resolution decreases noticeably. For the shear-waves the recovered slab fades significantly below about 250 km. The S-wave data do still detect a relative high around the deeper portion of the slab, but it is very diffusely represented.

Finally, Fig. 5a shows that the deeper low-velocity sphere located to the south is detected in both inversions. However, this recovered structure still displays significant diagonal smearing due to the limited spectrum of rays thereabouts.

Overall, the slab tests show that the three artificial structures are in principle identifiable in both models, but that the S-wave recovered model exhibits greater smearing at depth and more fading of the velocity anomaly within the slab itself. Moreover, the damped inversion procedure clearly underestimates the magnitudes of all three synthetic velocity anomalies. Although the recovered images have reduced contrast compared to the input models, it is still gratifying that there appears to be sufficient lateral, depth and out-of-plane resolution to recognize structures that are plausibly consistent with the experiment's tectonic setting.

5. Results

Our real-data tomographic images are presented in Figs. 4b–6b and 7. The upper mantle structures show velocity perturbations (relative to the IASPEI Earth model) of $\pm 1\%$ for both P- and S-wave speeds. Our final models indicate the presence of four main features, two negative and two positive velocity anomalies.

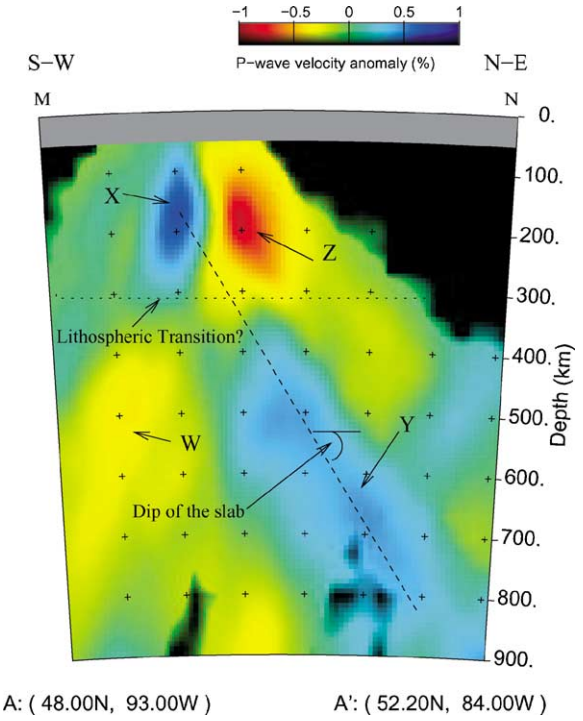

Fig. 7. Enlarged vertical cross-section across the P-wave model showing the main anomalies observed beneath the WSP. The location of the vertical cross-section MN is shown by a white line in the first horizontal section (Fig. 4a).

These structures appear to be geometrically similar in both the P- and S-wave images, even though they were independently obtained. The robust-inversion images explain 92% of the rms residual for P-wave arrivals (reduced from 0.25 to 0.02 s) and 93% of the S-wave arrivals (from 0.71 to 0.05 s). These levels are similar to ones obtained by Wolfe et al. (1997), VanDecar et al. (1995) and Rondenay et al. (2000).

Comparisons between the synthetic slab model images (Figs. 4a–6a) and the real-data models (Figs. 4b–6b) indicate that the earlier three test structures approximately reproduce the main velocity anomalies obtained from both the P- and S-wave datasets. Hence the synthetic model is one plausible representation of the actual upper mantle structure beneath the WSP and a useful starting point for the interpretation. The structures observed in our final models are evidently distinct from the surrounding mantle.

One prominent feature is a shallow (less than 300 km depth) high-velocity anomaly located beneath the Quetico–Wabigoon (Q–W) subprovinces. Consider, for example, the P-wave velocities in Fig. 4b at 150 km and sections MN and OP in Fig. 5b. At the south of section KL in Fig. 5b, a low-velocity feature V, not simulated in the slab resolution test, dominates the high-velocity feature just to its NE in the P-wave image (though not in the S-wave image). Taking the three NE-trending sections together, we conclude that in three dimensions the final tomographic results in this depth range are compatible with a roughly tabular-shaped velocity high oriented with a NW–SE strike. The dip is not well constrained over this ‘narrow’ depth interval and an estimate of its lateral extent beyond about 100 km cannot be made. In constraining the strike, though, it is worth noting the compatible orientation of the neighbouring low-velocity to its NE in Fig. 4b (at 150 km depth).

A second prominent positive P-wave anomaly lies at greater depth and further to the NE (around point Y in Fig. 7). Resolution test results in this vicinity, such as that along section CD in Fig. 3, indicate that the diagonal trend of this deeper P-wave high-velocity body is not due to strong smearing of a compact object (low diagonal resolution) and that it should be regarded as a robust feature. Indeed, several variations on the earlier slab resolution test were used to assess the probable depth extent of this dipping high-velocity anomaly. These variations used synthetic slabs extending down to 400, 500, 600 and 700 km (the latter being the example shown in Fig. 5a). The recovered images show that synthetic slabs extending to 400 and 500 km are not diagonally smeared strongly enough to generate reasonable agreement with our real-data highs at 800 km (Fig. 7). In contrast, the 700 km synthetic slab of Fig. 5a is too strongly smeared into the lower mantle and exits the model space to the NE with a very high amplitude at 800 km depth. The real-data images in Fig. 5b seem to fade before reaching this point. Our preferred fit to the real-data image of Fig. 7 would be obtained with a synthetic slab reaching to somewhere between 550+ and 700 km. This suggests that the deeper high-velocity feature may be trapped within the transition zone which separates the 410 and 660 km discontinuities.

In combination, the shallow and deep high-velocity structures suggest the presence of a larger slab-shaped anomaly cross-cut by a low-velocity perturbation, the shallow extreme of the latter being located below the Wabigoon subprovince (50°N, 89.5°W; around point Z in Fig. 7). The S-wave images in Fig. 5b do not show a strong slab high at depth, but this is consistent with the earlier test conclusions that below 200 km the S-wave resolution is poor.

The shallower negative anomaly just referred to is much clearer in the P-wave images of Fig. 5b than in the S-wave images. In section MN of the S-wave image in Fig. 5b, there is very significant smearing towards the NE as well as to the SW. This NE smearing occurs further north and deeper than 250 km, and hence is at the limit of the S-wave data resolution window previously identified. In contrast, the ‘smearing’ to the SW occurs centrally in the model (e.g. Fig. 5b; section MN) where resolution is better, especially for the P-wave image. The low-velocity anomaly serves to ‘pinch’ the ‘slab’ signature at around 300 km. The artificial low-velocity sphere used in the earlier resolution test reproduces well the anomaly observed in the real-data P-wave image and for the S-wave data the results are not too bad when the stronger exterior diagonal smearing towards the NE is considered. It is conceivable, then, that this low-velocity perturbation may be localized around 150 km depth and may impinge on the high-velocity slab.

Another negative (low-velocity) anomaly is observed below 400 km in the southern part of the seismic network, more explicitly beneath the

Wawa–Quetico–Wabigoon subprovinces (around point W in Fig. 7). This anomaly appears to have a roughly elliptical form, exiting the model space at the southern edge. The earlier slab model test showed that such an elongated shape in this location may simply be the result of significant smearing at depth and this deeper anomaly is also well modeled by a spherically-shaped structure. Note that this anomaly has a higher amplitude in the S-wave image (Fig. 5b).

Around the southernmost station (at point V in Fig. 5b; lower P-wave image), a smaller shallow low-velocity patch is observed down to 150–200 km. It is strongest in the P-wave structure. A separate resolution test using a high-velocity sphere centered at 200 km was performed to determine if this low may represent an artifact of the spline interpolation in the presence of strong lateral gradients from the high-velocity anomaly observed just to the north (i.e. from the shallow extreme of the inferred fast slab). The results of this test demonstrate that while the presence of strong gradients may create low-velocity artifacts on both sides of a high-velocity perturbation, these lows should appear closer to the main anomaly and be much smaller in magnitude and extent. For these reasons, this relative low-velocity zone should be considered real.

Finally, our models indicate that the region north of the English River subprovince (Fig. 1) extending to the center of the Sachigo does not contain any major velocity features (Fig. 4b; above 51.5°N). Still further north (beyond 53°N), the poor resolution obtained means that the low-velocity area observed (only) in the S-wave model around station BBT should not be overinterpreted (see Fig. 4b).

6. Discussion

In light of the geological setting, the existing evidence for subduction processes having occurred in the WSP, and the resemblance of the imaged dipping structure to images of modern-day subducting slabs, we consider the possibility that this feature may represent remnant subducted oceanic lithosphere, perhaps cross-cut by a shallow low-velocity zone. The resolution appears to be sufficient to ascribe a SE–NW strike to the slab, which when compared to the broadly EW strike of the main geology in the WSP is suggestive of subduction along a trench/margin that may be called ‘oblique’ (SW–NE, or at roughly 60° from north). This would be consistent with a transpressional environment, which was already suggested by SKS splitting interpretations (Silver and Chan, 1991; Kay et al., 1999). However, the appearance of a remnant slab as a coherent high-velocity feature when its age would presumably preclude the contribution of thermal contrasts to its seismic signature requires explanation. There are also other properties of the P- and S-wave images which should be considered. In Figs. 5b and 6b, for example, it is curious that the depth 300 km seems to mark a horizon across which the continuity of the proposed slab or its cross-cutting low-velocity feature are disturbed. There are also discrepencies between the P- and S-wave images at shallower depths which may be significant.

6.1. Remnant slab anomalies

The dipping high-velocity ‘slab’ anomaly is observed within the expected cratonic root and its extent may be terminated at the 660 km phase transition (Fig. 5b; P-wave image). The synthetic resolution tests indicate that a slab width of around 30–50 km is required for such a body to be tomographically visible (at least as it appears in Figs. 4b–6b). This might characterize a portion of remnant oceanic lithosphere that has been trapped by the base of the transition zone since the Archean. A low density contrast between the slab and the mantle below the 660 km ‘discontinuity’ may have prevented penetration into the lower mantle. The actual NS position of this fossil subducted slab, which might have been emplaced at 2.70 Ga, is in good agreement with one of the current interpretations of the Neoarchean tectonic evolution of the Superior Province (Langford and Morin, 1976; Card and Poulsen, 1998, Fig. 2.37 at the Quetico–Wabigoon boundary—what we may call the Q–W slab). In this interpretation, the accretionnary sequences originate from a series of northward-dipping subduction zones. The east–west pattern of volcanic belts within the WSP favours this accretionary evolution. An interesting point, though, is that the orientation of the remnant slab observed in our images indicates an oblique SW–NE subduction direction. Its particular (southerly) location suggests it was the last major event to affect the Superior Province, which may

enhance the possibility that such a slab could be still visible within the upper mantle.

If correctly interpreted, our results imply that in the upper mantle it is still possible to recognize some slabs which were subducted 2.7 billion years ago. An earlier observation to the west of our array using seismic reflection (Calvert et al., 1995) supports such slab visibility in the Superior Province. Their structure, extending 30 km below the Moho, was interpreted as a fossil suture associated with subduction and would be consistent with the presence of Archean plate-tectonic activity. The existence of remnants from Archean subduction has also been suggested by other techniques, for example, geochemical analysis of amphibolites from the Wyoming Province (Mueller and Wooden, 1988). Stability and detectability of remnant slabs within the transition zone after such a long residence time is generally unexpected. For example, Wen and Anderson (1997) demonstrated the good correlation between the presence of velocity anomalies in the transition zone with recent subduction (0–30 Ma) and a poor correlation after longer periods of time, arguing that an older slab would sink into the lower mantle. Nevertheless, they also suggest that thick cratonic roots may affect or modulate upper mantle convection. Beneath the Superior Province in particular, the 660 km seismic discontinuity may have acted as a barrier to convection and prevented material in the upper mantle from being reworked by convective flow. A complementary idea was proposed by Abbott et al. (1994), who argued that the thick Archean mantle root may prevent mantle upwelling. This would mean that the upper mantle has moved as a unit since the Archean. Similar coupling between the mantle root and the underlying upper mantle for a shorter period of time (130 Ma) has been suggested beneath South America by VanDecar et al. (1995).

The observation of velocity perturbations through tomographic studies may reflect either a compositional contrast, a thermal one or both. Stein and Stein (1996) argued via thermal modelling that after 100 Ma the slab/mantle temperatures should equilibrate, suggesting that the high-velocity anomaly observed could not have an original subduction-related thermal origin. We are, therefore, left to consider either some more-recent thermal origin or a compositional cause for this positive anomaly. While it is conceivable for ±1% lateral velocity variations over distances of several 100 km to arise from lateral temperature variations, there is no independent evidence for a current regional thermal regime that could easily account for the three-dimensional pattern or geometry of anomalies that we see. Hence, we focus now on compositional causes, such as the fossil interaction between an eclogite slab embedded in a harzburgite mantle by subduction.

Indeed, the upper part of the oceanic lithosphere composed mainly of hydrated gabbro and basalt will metamorphose first into blueschist facies and then into eclogite in the upper mantle. Our resolution tests indicate that a subducting body of thickness 30–50 km is required to reproduce our real-data anomaly and we note that according to Hoffman and Ranalli (1988) Archean oceanic crust might be significantly thicker than modern oceanic crust. This last hypothesis is based on the fact that mantle temperatures in the Archean must have been higher than at present day, resulting in large degrees of partial melting. Studies of xenoliths in kimberlites (e.g. Boyd and Gurney, 1986; or a more recent study by Schmidberger and Francis (1999) comparing mantle xenoliths in Archean terranes with those in younger terranes) corroborate the correspondingly more depleted nature of lithospheric mantle beneath Archean cratons. This could explain the velocity contrast observed between the proposed eclogite remnant slab and a neighbouring highly-depleted harzburgite. Babuska and Cara (1991, p. 65) provide a summary of seismic velocities of upper mantle rocks, showing the consistently-higher wave speeds of eclogites over harzburgites.

On the other hand, it may be unnecessary to invoke solely a thick Archean oceanic crust to explain our wide high-velocity slab anomalies. Theorized highly depleted Archean oceanic lithospheric mantle of dunite composition (Ringwood and Irifune, 1988; Ringwood, 1991) may add to the effect of the eclogite layer. According to Babuska and Cara (1991, p. 65) dunite velocities, like those of eclogite, would likely be higher than those of a harzburgite continental root underlying the WSP around our inferred ancient subduction zone.

6.2. Low-velocity anomalies

The presence of two strong low-velocity anomalies: (i) within the mantle wedge; and (ii) at great depth in the far south, could be explained by independent

or related mechanisms. In subduction zones, the sinking cold lithosphere may generate low velocities in the shallow mantle via dehydratation reactions and volatile-flux melting of the overlying mantle (Anderson et al., 1992). The water released at the edge of the descending slab may cause hydration reactions or more specifically serpentinization within the mantle wedge (Peacock, 1993; Fryer et al., 1985). The observation of our shallow low-velocity anomaly may then reflect the presence of compositional residue of serpentinite. Our slab resolution tests suggest that smearing of this shallower anomaly may be responsible for the interruption (pinching) of the dipping high-velocity remnant slab signature. If this mechanism correctly explains the shallow low-velocity zone, it implies that the deeper low-velocity anomaly is quite separate, possibly a local melting zone associated with post-Archean upwelling material.

The second possibility is that the shallow and deep low-velocity anomalies are connected. Even though our earlier resolution tests showed that the deeper low-velocity sphere may actually be quite far from the dipping Q–W slab (so that it is only the result of imperfect resolution which creates the impression that it impinges upon the latter), we cannot confidently exclude the possibility that in the real-data images the shallow and deep features are genetically linked. Indeed, inspection of Figs. 5b and 6b suggests the possibility of a plume cross-cutting the high-velocity slab. The orientations of the deep and shallow low-velocity anomalies appear to line up, so that rather than being highly localized they may be expressions of a continuous structure associated with mantle upwelling after the stabilization of the craton.

Finally, our study indicates that major velocity structures are absent beneath the reasonably-resolved Berens and southernmost Sachigo subprovinces (i.e. around stations B11–B14). The latter is the oldest and most stable part of the craton, and in earlier SKS work these stations also seemed to have coherent and distinct polarization orientations (Kay et al., 1999). Thus, our tomography images reinforce the impression that the upper mantle beneath the Caribou/Sachigo protocraton is significantly different from that under the accreted terranes to the south. Note that in our figures the vertical sections stop (at about 53°) just south of station BBT (Big Trout Lake) on account of the dimished resolution there.

6.3. The continental root

Further inspection of our final models leads to questions regarding the thickness of the continental root or such discrepancies as exist between the P- and S-wave models in the lithosphere. For instance, in Fig. 5b the extent in depth of the anomalies within the keel may allow us to estimate the thickness of the cratonic root at around 300 km. This is the depth at which all the anomalies within the upper part of the upper mantle seem to stop sharply.

Numerous previous studies have indicated the presence of a thick lithosphere beneath Archean cratons. A study made by Van der Lee (1997) using surface waves established that the Archean craton in North America may reach depths of 350 km. A heat flow study in the Canadian Shield by Jaupart et al. (1998) suggested a thermally-stable lithosphere of 240 km overlying a small-scale convection layer. On the other hand, compared with some other tomographic studies of cratonic lithosphere (e.g. Ritsema et al., 1998), the overall structure of the mantle lid of the WSP appears not to be a large, single, root-like feature contrasting strongly with a laterally-uniform asthenosphere.

Regarding the imperfect correspondence between the P- and S-wave velocity models, several causes may be considered. The discrepancies observed within the asthenosphere are attributable to the poorer resolution of the S-wave dataset and this may even be true within the lithosphere. For the latter, similar discrepancies were observed in studies beneath the Canadian Shield by Bokelmann and Silver (2000) and beneath central Iceland by Wolfe et al. (1997). The presence of partial melts associated with mantle anisotropy was suggested as a possible cause. Indeed, a travel time study from the APT89 experiment (Bokelmann and Silver, 2000) reveals large variations between P- and S-wave delays leading to a V_P/V_S ratio higher than 2.25. They argue that partial melting may be responsible for a ratio up to 2.25, but beyond this value seismic anisotropy must be taken into consideration. A study made at our stations by Kay et al. (1999) using SKS splitting analysis reveals large delay times and a fast polarization direction oriented roughly EW. These parameters confirm the presence of strong anisotropy beneath the WSP detected earlier by Silver and Chan (1991). This anisotropy is mostly attributed to lattice

preferred orientation of olivine crystals within a thick upper mantle layer of peridodites. Anisotropy was also found using P-wave phases from a refraction study along the same corridor (Musacchio et al., 1999). Both methods established a fast polarization direction oriented more-or-less parallel to the tectonic strikes. Although the presence of anisotropy is seemingly a fact beneath the WSP, it may have a limited impact on our tomographic images in view of the fair event azimuthal coverage and resulting averaging. We are, therefore, left to consider more favourably the other mechanisms for our tomographic image features, but ultimately an interpretation integrating SKS splitting, refraction, surface wave and tomographic results is required. A more complete overview has been given by Kendall et al. (in press).

Lastly, it may be wrong to assume that our apparent slab structure is stationary in the upper mantle. Helmstaedt and Schulze (1984) present a very graphic model (Fig. 3.8; see also Deines et al., 2001, Fig. 2) of continental root formation by imbrication of subducted plates. The possibility of one or more plates subsequently delaminating and sinking, due to changing conditions either in the mantle or lithosphere, could alleviate the need to explain an extreme longevity for our apparent slab structure at asthenospheric depths. Indeed, there are other scenarios once we consider the possibility of active structures. For example, if the apparent transition at around 300 km does represent the continental root extent, then the deeper lateral variations may be unrelated structures over which the craton has moved. The deeper apparent slab would then be just coincidentally positioned to give the impression of an alignment with shallower lithospheric features. That deeper structure may signify, for example, a small-scale convection cell (Jaupart et al., 1998; Kendall et al., in press) tilted by viscous drag from the overriding plate. While we must remain open to such possibilities, we prefer, at least for the purposes of future hypothesis testing, to focus here on interpretations that may relate more directly to the surface geology.

7. Conclusions

The inversion of P- and S-wave travel times beneath the WSP suggests the presence of three significant velocity anomalies. The first is a dipping tabular high-velocity anomaly that we may interpret as a 30–50 km thick eclogite/dunite layer. This high-velocity body, which may have been emplaced in late Archean times, could represent a remnant subducted oceanic lithosphere. The second and third anomalies are low-velocity features. The shallowest of these is plausibly associated with the dehydration processes that occur at the edge of a descending slab. The deeper one is possibly the effect of material that upwelled later into this region. We cannot exclude the possibility that the shallow and deep low-velocity anomalies are connected and represent a plume-like structure which penetrated the slab. Finally, our tomographic images contain a transition at around 300 km, which could reflect the thickness of the continental root.

Overall, our images are plausibly consistent with plate tectonic processes in the Archean. However, the SE–NW strike of the apparent remnant slab is in contrast with the EW trend of the subprovince-scale structure of Western Superior and may have implications that can be tested by other geological and geophysical studies.

Acknowledgements

Thanks to the First Nations of Big Trout Lake, Fort Severn and Peawanuck, and to Monopros Ltd., the Royal Society of London, the Geological Survey of Canada, NSERC and especially LITHOPROBE for their asssistance and support. We also thank Thunder Airlines (Dawn Traer) for logistical support. Dave Francis (Leeds) and Brian Roberts (GSC) are thanked for their contributions to data collection and compilation. Carl-Georg Bank and Stéphane Rondenay provided technical assistance with the methodology. Herb Helmstaedt and Rob Harrap gave feedback on the possible interpretations. A thorough GSC internal review by D. Snyder proved very helpful.

References

Abbot, D., Burgess, L., Longhi, J., Smith, W.H.F., 1994. An empirical thermal history of the Earth's upper mantle. J. Geophys. Res. 99, 13835–13850.

Anderson, D.L., Tanimoto, T., Zhang, Y., 1992. Plate tectonics and hotspots: the third dimension. Science 256, 1645–1651.

Babuska, V., Cara, M., 1991. Seismic Anisotropy in the Earth. Kluwer Academic Publishers, Dordrecht.

Bank, C.-G., Bostock, M.G., Ellis, R.M., Hajnal, Z., VanDecar, J.C., 1998. Lithospheric mantle structure beneath the Trans-Hudson Orogen and the origin of diamondiferous kimberlites. J. Geophys. Res. 103, 10103–10114.

Bokelmann, G.H.R., Silver, P.G., 2000. Mantle variation within the Canadian Shield: travel times from the portable broadband Archean–Proterozoic transect 1989. J. Geophys. Res. 105, 579–605.

Boyd, F.R., Gurney, J.J., 1986. Diamonds and the African lithosphere. Science 232, 472–477.

Brune, J., Dorman, J., 1963. Seismic waves and earth structure in the Canadian Shield. Bull. Seismol. Soc. Am. 53, 167–210.

Calvert, A.J., Sawyer, E.W., Davis, W.J., Ludden, J.N., 1995. Archean subduction inferred from seismic images of a mantle suture in the Superior Province. Nature 375, 670–674.

Card, K.D., Poulsen, K.H., 1998. Geology and mineral deposits of the Superior Province of the Canadian Shield. Geol. N. Am. Ser. 7, 15–204.

Cline, A.K., 1981. FITPACK-software package for curve and surface fitting employing splines under tension. Department of Computer Science, University of Texas at Austin.

Deines, P., Viljoen, F., Harris, J.W., 2001. Implications of the carbon isotope and mineral inclusion record for the formation of diamonds in the mantle underlying a mobile belt: Venetia, South Africa. Geochim. Cosmochim. Acta 65, 813–838.

Fouch, M.J., Fischer, K.M., Parmentier, E.M., Wysession, M.E., Clarke, T.J., 2000. Shear wave splitting, continental keels and patterns of mantle flow. J. Geophys. Res. 105, 6255–6276.

Fryer, P., Ambos, E.L., Hussong, D.M., 1985. Origin and emplacement of Mariana forearc seamounts. Geology 13, 774–777.

Grand, S.P., Helmberger, D.V., 1984. Upper mantle shear structure of North America. Geophys. J. R. Astron. Soc. 76, 399–438.

Helmstaedt, H., Schulze, D.J., 1984. Southern African kimberlites and their mantle sample: implications for Archean tectonics and lithosphere evolution. In: Kimberlites and Related Rocks. Proceedings of the Fourth International Kimberlite Conference, Geological Society of Australia Special Publication 14, Vol. 1. pp. 399–438.

Hoffman, P.F., Ranalli, G., 1988. Archean oceanic flake tectonics. Geophys. Res. Lett. 15, 1077–1080.

Hynes, A., 1999. Seismic reflections and the gravity field: indications of the deep structure of the Uchi, English River and Winnipeg River subprovinces. In: Harrap, R.M., Helmstaedt, H. (Eds.), LITHOPROBE Western Superior Transect Report 70. p. 80.

Jaupart, C., Mareschal, J.C., Guillou-Frottier, L., Davaille, A., 1998. Heat flow and thickness of the lithosphere in the Canadian Shield. J. Geophys. Res. 103, 15269–15286.

Kay, I., Sol, S., Kendall, J.-M., Thomson, C.J., White, D., Asudeh, I., Roberts, B., Francis, D., 1999. Shear wave splitting observations in the Archean craton of Western Superior. Geophys. Res. Lett. 26, 2669–2672.

Kendall, J.M., Sol, S., Thomson, C.J., White, D.E., Asudeh, I., Snell, C.S., Sutherland, F.H. Seismic heterogeneity and anisotropy in the Western Superior Province, Canada: insights into the evolution of an Archaean craton. In: Fowler, C.M.R., et al. (Eds.), The Early Earth: Physical, Chemical and Biological Development. Special Publications 199, Geological Society, London, in press.

Kennett, B.L.N., Engdahl, E.R., 1991. Travel times for global earthquake location and phase identification. Geophys. J. Int. 105, 429–465.

Langford, F.F., Morin, J.A., 1976. The development of the Superior Province of northwestern Ontario by merging island arcs. Am. J. Sci. 276, 1023–1034.

Mueller, P.A., Wooden, J.L., 1988. Evidence for Archean subduction and crustal recycling, Wyoming Province. Geology 16, 871–874.

Musacchio, G., White, D.J., Asudeh, I., Thomson, C.J., 1999. Lithospheric structure of Western Superior Province. Eos Trans. Am. Geophys. Union 8046, 1030.

Peacock, S.M., 1993. Large-scale hydration of the lithosphere above subducting slabs. Chem. Geol. 108, 49–59.

Ringwood, A.E., 1991. Phase transformations and their bearing on the constitution and dynamics of the mantle. Geochem. Cosmochem. Acta 55, 2083–2110.

Ringwood, A.E., Irifune, T., 1988. Nature of the 650 km seismic discontinuity: implications for mantle dynamics and differentiation. Nature 331, 131–136.

Ritsema, J., Nyblade, A.A., Owens, T.J., Langston, C.A., VanDecar, J.C., 1998. Upper mantle seismic velocity structure beneath Tanzania east Africa: implications for the stability of cratonic lithosphere. J. Geophys. Res. 103, 21201–21213.

Rondenay, S., Bostock, M.G., Hearn, T.H., White, D.J., Ellis, R.M., 2000. Lithospheric assembly and modification of the SE Canadian Shield: Abitibi–Grenville teleseismic experiment. J. Geophys. Res. 105, 13735–13754.

Schmidberger, S., Francis, D., 1999. Nature of the mantle roots beneath the North American craton: mantle xenolith evidence from Somerset Island kimberlites. Lithosphere 48, 195–216.

Silver, P.G., Chan, W.W., 1991. Shear wave splitting and subcontinental mantle deformation. J. Geophys. Res. 96, 16429–16454.

Stein, S., Stein, C.A., 1996. Thermomechanical evolution of oceanic lithosphere: implications for the subduction process and deep earthquakes. Subduction: top to bottom. Geophys. Monogr. Am. Geophys. Union 96, 1–17.

Van der Lee, S., Nolet, G., 1997. Upper mantle S-wave velocity structure of North America. J. Geophys. Res. 102, 22815–22838.

VanDecar, J.C., 1991. Upper mantle structure of the Cascadia subduction zone from non-linear teleseismic travel time inversion. Ph.D. thesis, University of Washington, Seattle.

VanDecar, J.C., Crosson, R.S., 1990. Determination of teleseismic relative phase arrival times using multi-channel cross-correlation and least-squares. Bull. Seismol. Soc. Am. 80, 150–169.

VanDecar, J.C., James, D.E., Asumpcao, M., 1995. Seismic evidence for a fossil mantle plume beneath South America and implications for plate driving forces. Nature 378, 25–31.

Wen, L., Anderson, D.L., 1997. Slabs, hotspots, cartons and mantle convection revealed from residual seismic tomography in the upper mantle. Phys. Earth Planetary Interiors 99, 131–143.

White, D.J., Helmstaedt, H., Harrap, R., Van der Velden, A., Hall, K., 1999. Architecture of Neoarchean crust: preliminary results from deep seismic profiling in the Western Superior Province, Canada. Eos Trans. Am. Geophys. Union 8046, 976–977.

Wolfe, C.J., Bjarnason, I.T., VanDecar, J.C., Solomon, S.C., 1997. Seismic structure of the Iceland mantle plume. Nature 385, 245–247.